

Critical role of hydrogen for superconductivity in nickelates

<https://doi.org/10.1038/s41586-022-05657-2>

Received: 6 May 2022

Accepted: 14 December 2022

Published online: 1 March 2023

 Check for updates

Xiang Ding^{1,9}, Charles C. Tam^{2,3,9}, Xuelei Sui^{4,9}, Yan Zhao¹, Minghui Xu¹, Jaewon Choi², Huaqian Leng¹, Ji Zhang⁵, Mei Wu⁶, Haiyan Xiao¹, Xiaotao Zu¹, Mirian Garcia-Fernandez², Stefano Agrestini², Xiaoqiang Wu⁷, Qingyuan Wang^{7,8}, Peng Gao⁶, Sean Li⁵, Bing Huang^{4,8}, Ke-Jin Zhou^{2,8} & Liang Qiao^{1,8}

The newly discovered nickelate superconductors so far only exist in epitaxial thin films synthesized by a topotactic reaction with metal hydrides¹. This method changes the nickelates from the perovskite to an infinite-layer structure by deintercalation of apical oxygens^{1–3}. Such a chemical reaction may introduce hydrogen (H), influencing the physical properties of the end materials^{4–9}. Unfortunately, H is insensitive to most characterization techniques and is difficult to detect because of its light weight. Here, in optimally Sr doped Nd_{0.8}Sr_{0.2}NiO₂H epitaxial films, secondary-ion mass spectroscopy shows abundant H existing in the form of Nd_{0.8}Sr_{0.2}NiO₂H_x ($x \cong 0.2–0.5$). Zero resistivity is found within a very narrow H-doping window of $0.22 \leq x \leq 0.28$, showing unequivocally the critical role of H in superconductivity. Resonant inelastic X-ray scattering demonstrates the existence of itinerant interstitial s (IIS) orbitals originating from apical oxygen deintercalation. Density functional theory calculations show that electronegative H[−] occupies the apical oxygen sites annihilating IIS orbitals, reducing the IIS–Ni 3d orbital hybridization. This leads the electronic structure of H-doped Nd_{0.8}Sr_{0.2}NiO₂H_x to be more two-dimensional-like, which might be relevant for the observed superconductivity. We highlight that H is an important ingredient for superconductivity in epitaxial infinite-layer nickelates.

In 2019, Danfeng Li et al. reported unconventional superconductivity in infinite-layer Nd_{0.8}Sr_{0.2}NiO₂ films with a maximum superconducting temperature (T_c) of roughly 15 K. Although substantial progress has been achieved, such as the discovery of the hole-doped superconducting phase diagram^{10,11}, antiferromagnetic correlations^{12–15}, superconductivity in Nd₆Ni₅O₁₂ (ref. 16), charge density waves (CDW)^{17–19} the field is still in its infancy. One of the key challenges lies in material synthesis as superconductivity so far exclusively happens in epitaxial films, and only a few groups worldwide can reproduce superconducting nickelates^{1,2,10,11,16,18,20–22}. Nickelates show strong similarities to cuprates in structure, electronic and magnetic correlations, which raises the question as to whether a similar pairing mechanism applies here and how high a T_c could be achieved for nickelate superconductors.

To realize the ultra-low valence Ni¹⁺ in nickelates, requires strong topotactic reduction, for example, through the metal-hydride CaH₂ agent^{1–3}, that, however, may introduce unintentional H doping. Identifying and overcoming the issue of H in materials are the key steps for both scientific research and industrial applications: for example, realizing nitride-based LEDs²³. Although some have considered the effect of H (refs. 24–26) in nickelate superconductors (Supplementary Note 1), it is (1) unclear whether H actually exists in the infinite-layer nickelate thin films? and (2) if so, what role does H play in superconductivity?

H identification and quantification

To answer these questions, we designed a series of experiments to characterize the optimal 20% Sr-doped NdNiO₂ (Supplementary Note 2). Pulsed laser deposition was used to grow 15-nm-thick Nd_{0.8}Sr_{0.2}NiO₃ films epitaxially on a SrTiO₃(001) substrate (Methods and Extended Data Fig. 1)²⁷. As-grown Nd_{0.8}Sr_{0.2}NiO₃ films were reduced by CaH₂ at 300 °C under variable annealing times from 1 to 420 min (Methods). X-ray diffraction (XRD) spectra indicate the films are fully transformed from the perovskite into the infinite-layer structure (Extended Data Fig. 2). Ultra-sensitive secondary-ion mass spectroscopy (SIMS) was used to characterize the elemental distributions²⁸. Figure 1a shows that H is clearly detected with a strong signal in the bulk of all films. Its intensity becomes two orders of magnitude higher than the background level of as-received and reduced (300 °C, 120 min) SrTiO₃ crystals (Supplementary Note 3). Figure 1b shows typical three-dimensional (3D) SIMS element maps of a reduced superconducting sample (Extended Data Fig. 3). For all infinite-layer nickelates, the H distribution shows traces of diffusion into the substrate. These results unambiguously demonstrate the existence of abundant H in the infinite-layer nickelate, forming Nd_{0.8}Sr_{0.2}NiO₂H_x.

A pristine Nd_{0.8}Sr_{0.2}NiO₃ film also shows a notable H signal above the background level (Fig. 1a). The as-grown film was not treated by CaH₂

¹School of Physics, University of Electronic Science and Technology of China, Chengdu, China. ²Diamond Light Source, Harwell Campus, Didcot, UK. ³H. H. Wills Physics Laboratory, University of Bristol, Bristol, UK. ⁴Beijing Computational Science Research Center, Beijing, China. ⁵School of Materials, University of New South Wales, Sydney, New South Wales, Australia. ⁶International Center for Quantum Materials and Electron Microscopy Laboratory, School of Physics, Peking University, Beijing, China. ⁷Institute for Advanced Study, Chengdu University, Chengdu, China. ⁸Department of Physics, Beijing Normal University, Beijing, China. ⁹These authors contributed equally: Xiang Ding, Charles C. Tam, Xuelei Sui. ✉e-mail: wangqy@cdu.edu.cn; bing.huang@csr.ac.cn; kejin.zhou@diamond.ac.uk; liang.qiao@uestc.edu.cn

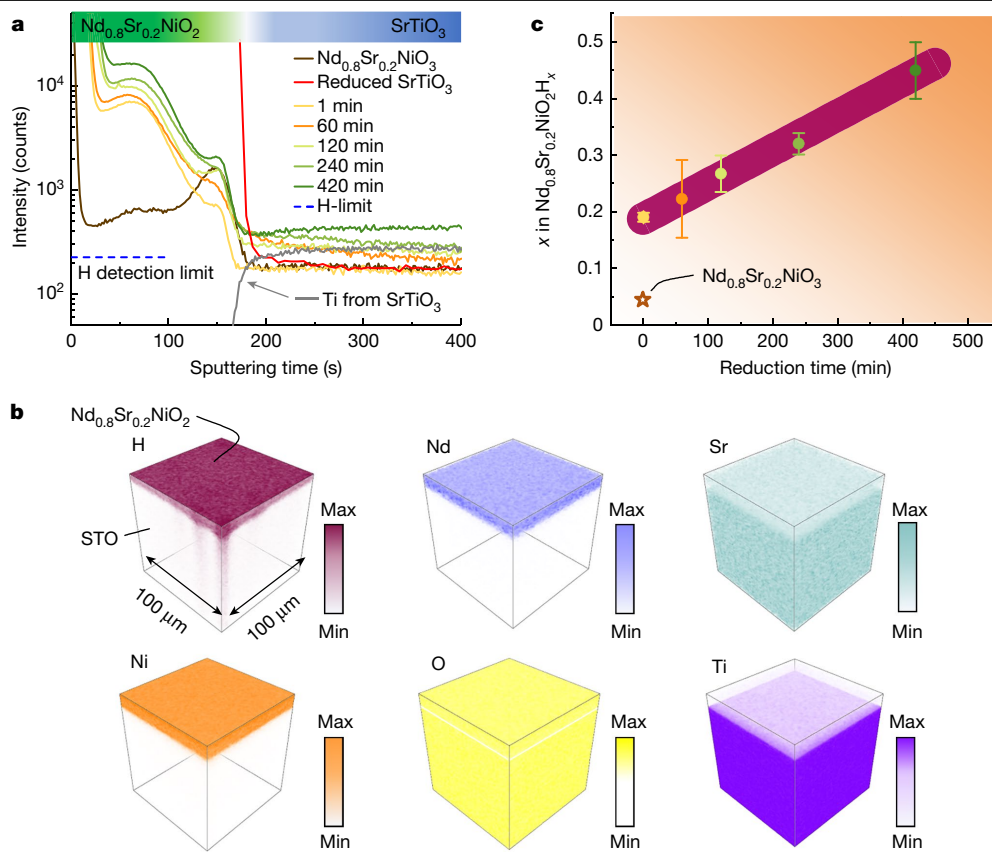


Fig. 1 | Hydrogen detection of as-grown and infinite-layer nickelates.

a, SIMS depth-profiles of pristine $\text{Nd}_{0.8}\text{Sr}_{0.2}\text{NiO}_3$ and $\text{Nd}_{0.8}\text{Sr}_{0.2}\text{NiO}_2$ films under different reduction times, along with a reference reduced SrTiO_3 single crystal using the optimized topotactic reduction condition of 300°C and 120 min (red solid line). The Ti signal from the SrTiO_3 substrate was used as a marker for the interface position. H detection limit (blue dashed line) was determined by

suggesting other sources such as residual water or H_2 trapped in the growth chamber²⁹. Furthermore, H was found in the polycrystalline $\text{Nd}_{0.8}\text{Sr}_{0.2}\text{NiO}_3$ target (Supplementary Note 4). Therefore, unintentional H could originate from the target, growth and the reduction process.

We choose natural mica, $\text{KAl}_2[\text{AlSi}_3\text{O}_{10}](\text{OH})_2$, as a reliable solid-state reference to quantify the H concentration in $\text{Nd}_{0.8}\text{Sr}_{0.2}\text{NiO}_2\text{H}_x$ (Methods and Extended Data Fig. 4). Figure 1c shows that the H concentration (x) increases linearly with the reduction time. The retrieved x falls in the range of $0.2 \cong 0.5$. This is similar to reported x values for other H-containing infinite-layer systems, such as SrVO_2H_x (ref. ⁴), SrCrO_2H_x (ref. ⁵), the H-containing perovskite systems BaTiO_3H_x (ref. ⁶), CaTiO_3H_x (ref. ⁷), $\text{LaSrCoO}_3\text{H}_x$ (ref. ⁸) and the H-containing pnictides $\text{SmFeAs}(\text{O}_{1-x}\text{H}_x)^z$. We highlight that the variation of H in $\text{Nd}_{0.8}\text{Sr}_{0.2}\text{NiO}_2\text{H}_x$ results from CaH_2 reduction rather than during the growth or from the $\text{Nd}_{0.8}\text{Sr}_{0.2}\text{NiO}_3$ target as both of which introduce a fixed level of H.

H-induced superconducting phase diagram

Figure 2a shows the temperature-dependent resistivity $\rho(T)$ of $\text{Nd}_{0.8}\text{Sr}_{0.2}\text{NiO}_2\text{H}_x$ samples, with x ranging from 0.19 to 0.44, respectively. A zoomed-in $\rho(T)$ curve below 30 K is shown in Extended Data Fig. 5. Obviously, the transport properties and superconducting transitions are systematically correlated with x , which can be constructed into a H-doping phase diagram (Fig. 2b). It depicts a superconducting dome with a narrow range of optimal H doping, $0.22 \leq x \leq 0.28$. Both under- and over-doped samples show weakly insulating behaviour with distinctive metal-insulator transition (MIT) temperature T_{MIT} , at

the as-received SrTiO_3 substrate. **b**, 3D mappings of H, Nd, Sr, Ni, O and Ti elements in a 120 min-reduced superconducting sample. The analysis area is $100 \times 100 \mu\text{m}^2$. **c**, Quantified hydrogen concentration as a function of reduction time. The star indicates the H concentration of pristine $\text{Nd}_{0.8}\text{Sr}_{0.2}\text{NiO}_3$. Mean \pm s.d. ($n = 3$) are shown.

which $d\rho/dT = 0$. The phase diagram shows a striking resemblance to that of the Sr-doped $\text{Nd}_{1-x}\text{Sr}_x\text{NiO}_2$ (refs. ^{10,11}) and demonstrates that, in addition to Sr dopant, a hidden H-dopant may play a critical role to the observed superconductivity. This may also explain the challenge of film synthesis, that is, H content must fall into a narrow window to achieve superconductivity.

To characterize the charge carriers upon H doping, we measured the Hall coefficient (R_H). Clearly, an electron-type conduction prevails in most of the doping and temperature range except the superconducting samples ($x = 0.24, 0.26$ and 0.28) exhibiting an electron-to-hole type conversion near 40 K (Fig. 2c). We also extracted R_H at 15 K and 300 K as a function of x (Fig. 2d). At 15 K, only optimally H-doped samples in the superconducting dome show hole conduction, whereas both under- and over-doped samples manifest the electron type. R_H at 300 K is electron-like and remains constant for most samples. Hall coefficients data suggest that both the electron and hole band are at play akin to the case of Sr doping^{1,10,11}. However, unlike with Sr doping, H doping seems to only have an effect at low-temperature rather than room-temperature R_H , whereas both low- and room-temperature R_H are responsive to Sr doping.

X-ray absorption spectroscopy (XAS) and resonant inelastic X-ray scattering (RIXS) experiments

XAS and RIXS were used to probe the electronic structure evolution upon H doping. Figure 3a shows the surface-sensitive O K -edge XAS spectra in total electron yield mode for $\text{Nd}_{0.8}\text{Sr}_{0.2}\text{NiO}_2\text{H}_x$ with $x = 0.19, 0.26$ and 0.33 , representative for under-doped, optimally doped

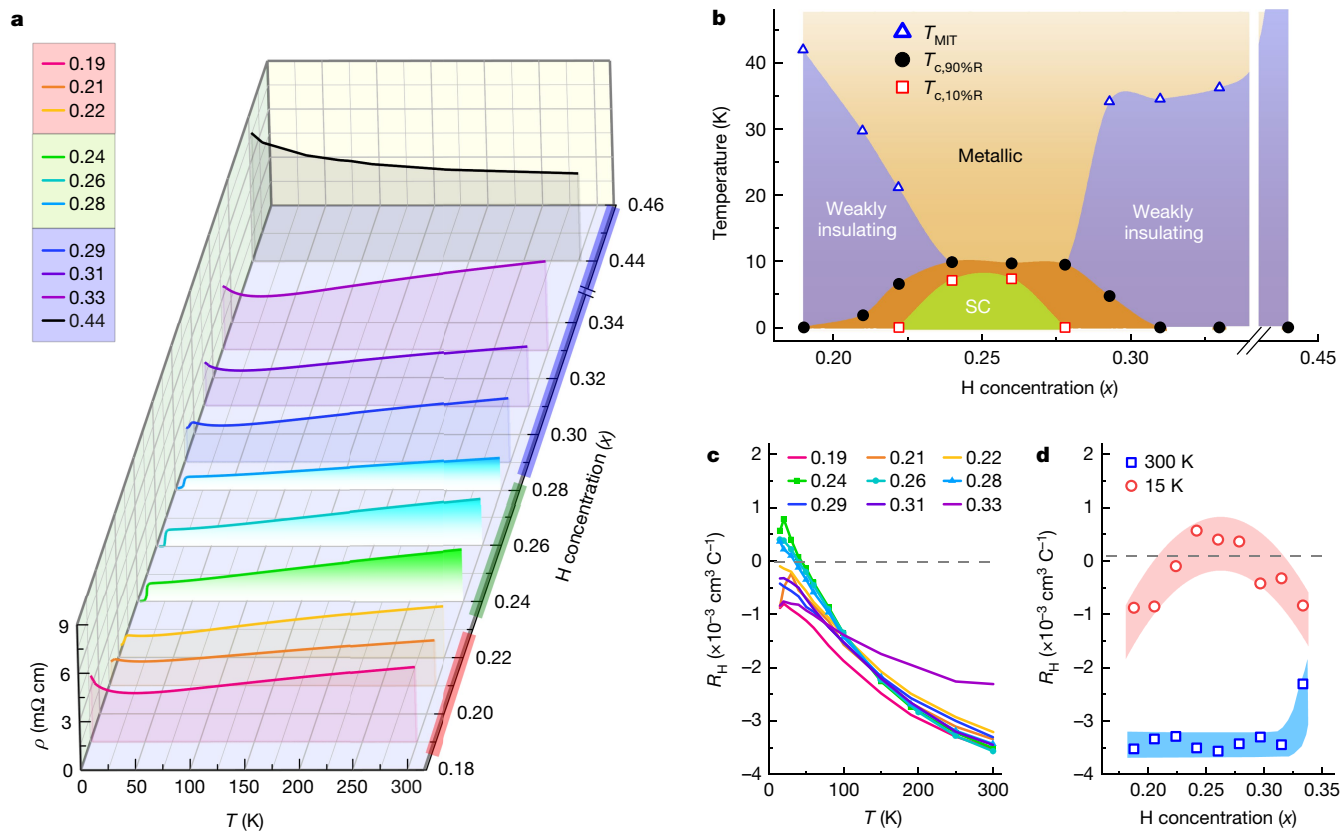


Fig. 2 | Transport properties and H-doping phase diagram of $\text{Nd}_{0.8}\text{Sr}_{0.2}\text{NiO}_2\text{H}_x$. **a**, Temperature-dependent resistivity measured for samples with different H concentrations (x from 0.19 to 0.44). For the small x value (0.19) and the large x values (0.31, 0.33 and 0.44), a weakly insulating behaviour is found with resistivity upturn of roughly 30 K. In intermediate ranges (0.21, 0.22 and 0.28, 0.29), a superconducting-like resistivity transition occurs, but zero resistance

and over-doped samples. The pre-edge peak at roughly 527–530 eV reflects the valence O $2p$ hole states and its mixing with $\text{Ni}^+ 3d$ orbitals. Comparing to perovskite NdNiO_3 , it reduces substantially in accord with other infinite-layer nickelates^{2,30}. The subtle change of the pre-peak among $\text{Nd}_{0.8}\text{Sr}_{0.2}\text{NiO}_2\text{H}_x$, suggests that the hole state and the O $2p$ – $\text{Ni} 3d$ hybridization may be slightly altered upon H doping. The $\text{Ni } L_3$ -XAS and RIXS spectra closely resemble those from $\text{R}_{1-x}\text{Sr}_x\text{NiO}_2$ ($\text{R} = \text{La, Nd, Pr}$) including the XAS spectral profile, the roughly 0.6 eV RIXS excitation manifesting significant $\text{Ni } 3d$ – $\text{Nd } 5d$ hybridization, the RIXS dd orbital excitations at roughly 1.1 eV, and fluorescence excitation^{2,12,17,18,30–32} (Fig. 3b,c and Supplementary Note 5). Closer inspection shows that the RIXS dd orbital excitations undergo a monotonic shift to lower-energy position as a function of x (Fig. 3c) consistent with the case of Sr hole-doping³¹ albeit to a smaller extent (Supplementary Note 7).

A distinct RIXS excitation appears in the optimal-doped ($x = 0.26$) sample at an incident energy roughly 2 eV above the rising absorption edge (circled area in Fig. 3e). Most of the $3d^{9-6}$ ground state allows us to compare the $\text{Ni } L_3$ -XAS with the calculated density of states (DOS) from which we assign the excitation to the hybridized state between $\text{Ni } 3d$ and itinerant interstitial s (IIS) orbitals (Supplementary Note 6). The IIS has been demonstrated in many non-oxide systems, such as layered compounds³³, electrides³⁴ and covalent semiconductors³⁵, which may strongly influence the fundamental electronic, topological and catalytic properties³⁶. For infinite-layer nickelates, IIS orbitals were theoretically predicted to locate at the interstitial apical oxygen vacancy (AOV) sites with an isotropic s -orbital-like DOS and major intensity roughly 2 eV above the Fermi level (E_f) (Fig. 4a)^{37,38}. The assignment is corroborated by the isotropic intensity of the IIS excitation

cannot be achieved. For the x range of $0.24 < x < 0.26$, the zero-resistance superconducting state is obtained. **b**, Phase diagram of $\text{Nd}_{0.8}\text{Sr}_{0.2}\text{NiO}_2\text{H}_x$. Circles (squares) represent 90% (10%) of the resistivity (R) value at 30 K. Open triangles represent the MIT temperature. **c**, Temperature dependence of R_H for the $\text{Nd}_{0.8}\text{Sr}_{0.2}\text{NiO}_2\text{H}_x$ thin films corresponding to **a**. **d**, The R_H at $T = 300$ and 15 K as a function of H concentration x .

extracted from polarization-dependent RIXS (Supplementary Note 6). The appearance of IIS excitations in the superconducting sample but not others indicate potentially an intimate connection among H doping, IIS orbitals and superconductivity.

Electronic structure of $\text{Nd}_{0.8}\text{Sr}_{0.2}\text{NiO}_2\text{H}_x$

SIMS is only sensitive to the mass of elements and is unable to determine the location of doped H and its valence state, that is, whether it is H^+ or H^- . Unfortunately, H in our samples cannot be observed by a transmission electron microscope (Supplementary Note 18). To understand these questions, density functional theory (DFT) was used (Methods). We examined configurations with H at various interstitial positions and identified that H prefers to occupy AOV forming a NiO_4H_2 local environment. Calculations of the scenario of hydroxide (OH^-) where H and O are bonded together yield a highly unstable structure (Supplementary Notes 8 and 9). The calculated partial DOS suggests H is in the form of electronegative H^- , consistent to many H-doped transition-metal oxides deintercalated using topotactic reduction (Supplementary Notes 10 and 11). This is also in line with RIXS spectra in which holes are introduced by H doping (Fig. 3c). In terms of the total energy calculations, we found that H prefers to form an ordered H–Ni–H chain along the out-of-plane direction but with no strong preference for the in-plane ordering state (Extended Data Fig. 6 and Supplementary Note 12).

To understand the electronic structure evolution induced by H doping, we calculated the band structure with orbital projections for three H concentrations $x = 0, 0.25$ and 0.5 (Fig. 4a–c). Overall, the IIS band clearly exists near E_f corresponding to the electronic states of AOV.

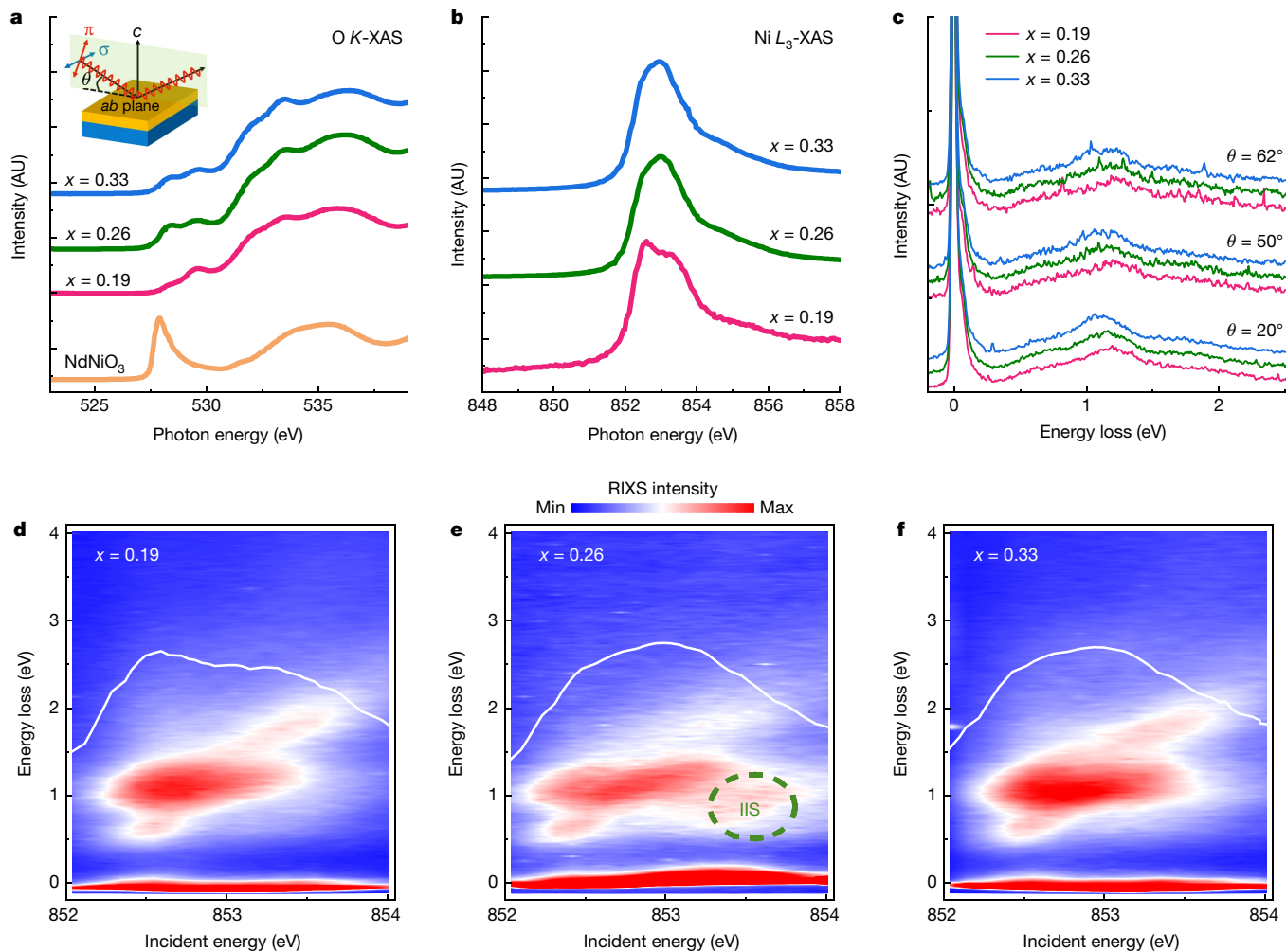


Fig. 3 | XAS and RIXS characterization. **a**, Surface-sensitive total electron yield XAS spectra near the O K -edge for $\text{Nd}_{0.8}\text{Sr}_{0.2}\text{NiO}_2\text{H}_x$ with $x = 0.19, 0.26$ and 0.33 , as well as the reference NdNiO_3 film. The experimental geometry is shown in the inset, where X-rays are incident on the film surface at a grazing angle θ with linear vertical (σ) and linear horizontal (π) polarization. AU, arbitrary units. **b**, Bulk-sensitive fluorescence yield XAS spectra near the Ni L_3 -edge

corresponding to **a, c**. Doping-dependent RIXS spectra under different incident angles θ . **d–f**, RIXS intensity map of $\text{Nd}_{0.8}\text{Sr}_{0.2}\text{NiO}_2\text{H}_x$ measured at $T = 20$ K with $x = 0.19$ (**d**), 0.26 (**e**) and 0.33 (**f**), respectively. The corresponding XAS are superimposed (solid white line) on top of each map. The IIS feature is highlighted as a dashed-green circle in **e**.

H doping annihilates the IIS band, which induces a rapid shift of its DOS towards higher energy and density reduction as reflected in the band structure. On the other hand, H doping alters the NiO_4 local environment and correspondingly the electronic structure. The deintercalation of apical oxygens changes the crystal field from O_h to D_{4h} symmetry, resulting in nearly fully occupied $3d_{z^2}$ orbitals with a partially filled $3d_{x^2-y^2}$ ground state. At the NiO_4H_2 local sites, H doping obliterates IIS band. The H 1s hybridizes with the $3d_{z^2}$ orbital of the nearest-neighbour forming a bonding-antibonding state, which pushes the antibonding $3d_{z^2}$ across E_F , hence reducing its orbital filling (Fig. 4a–c and Supplementary Notes 13 and 14). H doping seems to show little effect on the total $3d$ orbital filling and, consequently, the Ni $3d_{x^2-y^2}$ band shifts downwards in energy, demonstrating an increased orbital filling (Supplementary Notes 13).

The local orbital hybridization shows a complex but interesting development on H doping. The intra- and intercell atomic hopping energy and onsite energy difference were calculated using Wannier functions (Supplementary Notes 15). Among all, the nearest-neighbour hopping and the longer-range hopping terms are listed in Extended Data Table 1. Without the presence of H, the Ni $3d_{x^2-y^2}$ orbital couples strongly with the adjacent O $2p$ orbitals ($t_1 = 1.32$ eV), whereas Ni $3d_{z^2}$ –Nd $5d_{z^2}$ ($t_4 = 0.23$ eV) coupling shows much less strength. The IIS

orbital couples relatively strongly with both O $2p$ ($t_2 = -0.63$ eV) and Ni $3d_{x^2-y^2}$ ($t_3 = -0.21$ eV) orbitals. t_3/Δ_3 and t_4/Δ_4 are comparable, indicating the comparable orbital hybridization strength between $3d$ -IIS and $3d$ - $5d$. On H doping, the striking change is the diminishing of the hopping pathways to IIS orbitals, that is, t_2 and t_3 reduce to zero (Fig. 4d). Moreover, whereas Ni $3d_{x^2-y^2}$ –O $2p$ orbital coupling is not much affected by H doping, the hybridization between Ni $3d_{z^2}$ and Nd $5d_{z^2}$ orbitals weakens ($t_4 = 0.23 \rightarrow 0.06$ eV) (Supplementary Notes 15).

Discussion

The H-doping phase diagram of $\text{Nd}_{0.8}\text{Sr}_{0.2}\text{NiO}_2\text{H}_x$ is intriguing. The appearance of the superconducting dome in the optimal H doping range ($x = 0.2$ – 0.3) as well as the weakly insulating behaviour at both the under- and over-doped regimes ($x < 0.2$ and $x > 0.3$) almost mimic the hole-doping phase diagram of infinite-layer nickelate superconductors. This suggests that, besides the Sr dopant, H may play a critical role in superconductivity. At first glance, H may act just as a donor of ordinary charge carriers into the charge reservoirs, however, Hall coefficient, X-ray spectroscopy and DFT calculations demonstrate that the situation is more complex. For instance, although both the electron and hole types of carrier exist in the superconducting samples, Hall coefficients

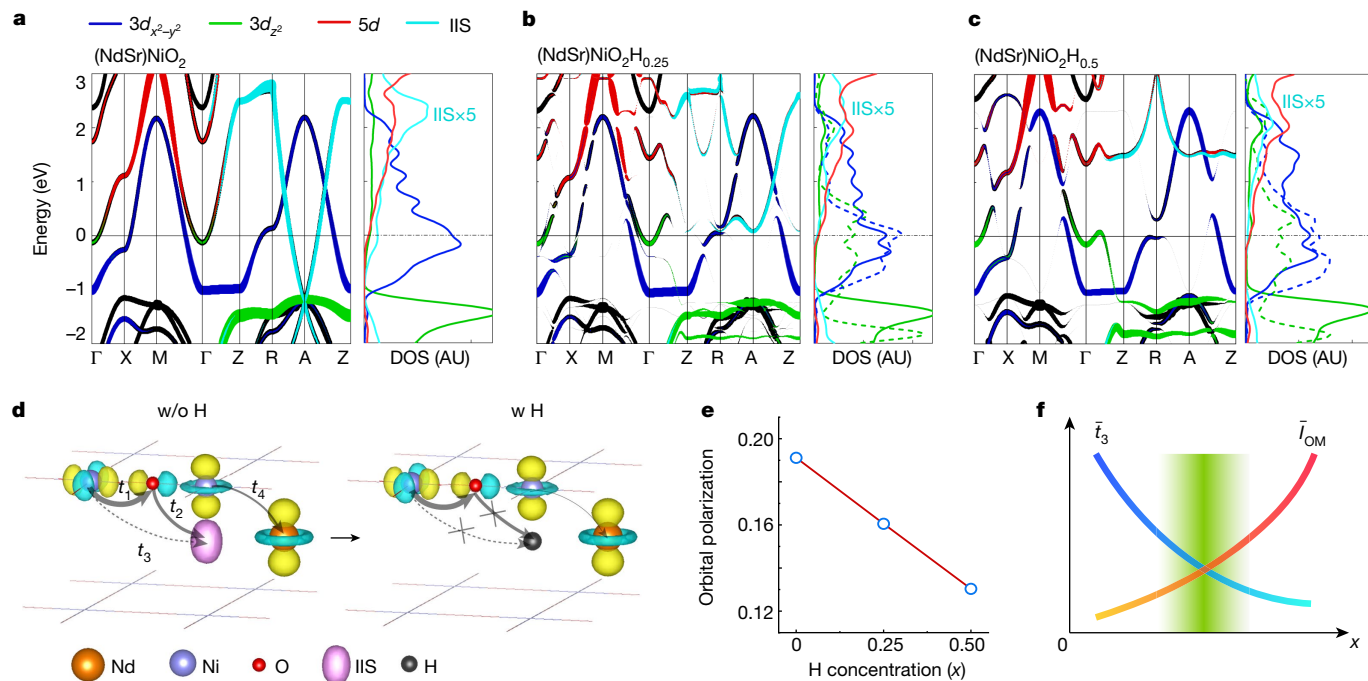


Fig. 4 | Electronic structure of $\text{Nd}_{0.8}\text{Sr}_{0.2}\text{NiO}_2\text{H}_x$. **a–c**, Band structures and DOS with orbital projections for $\text{Nd}_{0.8}\text{Sr}_{0.2}\text{NiO}_2\text{H}_x$ ($x=0$ (**a**), 0.25 (**b**) and 0.5 (**c**)) (corresponding structures are shown in Extended Data Fig. 6). The solid (dashed) lines in DOS are for the $3d$ orbitals in the NiO_4 (NiO_4H_2) environment. The DOS of IIS is enlarged by five times for clarity. Note that the IIS state is fully suppressed in the NiO_4H_2 environment. The Fermi level is set to zero. **d**, Intracell hopping (t_1 ($\text{Ni } 3d_{x^2-y^2} \rightarrow \text{O } 2p$), t_2 ($\text{O } 2p \rightarrow \text{IIS}$), t_4 ($\text{Ni } 3d_{z^2} \rightarrow \text{Nd } 5d_{z^2}$)) and intercell hopping (t_3 ($\text{Ni } 3d_{x^2-y^2} \rightarrow \text{IIS}$)) without (w/o, left) and with (w, right) the insertion of H in

$\text{Nd}_{0.8}\text{Sr}_{0.2}\text{NiO}_2\text{H}_x$. The weight of arrows represents the hopping strength, where the corresponding hopping energy t and onsite energy difference Δ are listed in Extended Data Table 1. A full table of t and Δ between more orbitals can be found in Supplementary Note 15. **e**, $3d_{x^2-y^2}-3d_{z^2}$ orbital polarization as a function of H concentration. Details can be found in Supplementary Note 13. **f**, Schematic drawing of the competition between the average $3d_{x^2-y^2}-3d_{z^2}$ orbital mixture (I_{OM}) and the average hopping \bar{t}_3 as a function of H concentration x , leading to an optimized x region (green-shaded region) that is more quasi 2D like.

deviate from what was observed in Sr-doped counterparts alluding to an extraordinary effect.

Besides confirming the $3d^{9-d}$ ground state, RIXS shows the IIS excitation is present only in the superconducting sample. It is not fully clear why the IIS excitation is not present at other H dopings which deserves further study. However, for the under-doped case, it may not be impossible that the IIS excitation overlaps with dd excitations because its central DOS are lower in energy intersecting $\text{Ni } 3d_{x^2-y^2}$ band. For the over-doped sample, with more H doping, IIS bands shift up in energy and reduce their weight, which perhaps explains its negligible contribution. DFT calculations indicate that the total $3d$ orbital filling is slightly changed, much less than expected according to the number of doped holes (Supplementary Notes 13). This seems at odds at first, however, the RIXS dd excitations indeed signal a modest energy shift as a response to a partial doping into $\text{Ni } 3d$ bands. The increased hole-peak intensity in the OK-XAS upon H doping probably underlines the involvement of $\text{O } 2p$ orbitals in the hole-doping, similar to the case of $\text{La}_4\text{Ni}_3\text{O}_8$ trilayer nickelate³⁹. Further studies are needed and may renew the view that the infinite-layer nickelates predominantly bear Mott–Hubbard physics².

Another small but important detail is the relevance of H doping to CDWs. In our RIXS spectra, no signs of CDWs show in any samples measured (Extended Data Fig. 7), consistent to the results in roughly 20% Sr-doped infinite-layer nickelates^{17–19}. The fact that CDWs progressively fade away with Sr doping in both LaNiO_2 and NdNiO_2 , regardless of the different growth conditions^{17–19}, suggests that H doping, if it exists, may not be the precursor of CDWs.

Finally, putting all the pieces together, we can draw a mechanism partially responsible for the H-doping phase diagram. Starting from the non-doped $\text{Nd}_{0.8}\text{Sr}_{0.2}\text{NiO}_2\text{H}_x$ ($x=0$), electron-like bands dominate with sizeable interlayer hopping and hybridization among IIS, $\text{O } 2p$,

$\text{Nd } 5d$ and $\text{Ni } 3d_{x^2-y^2}$ orbitals that lead to more 3D-like electronic structure. H doping blocks the interlayer hopping related to IIS orbitals rendering the electronic structure to be more quasi two-dimensional (2D)-like (Fig. 4d). On further H doping, the local crystal field and strong orbital coupling re-adjust the $\text{Ni } 3d$ states such that the $3d_{x^2-y^2}-3d_{z^2}$ orbital polarization (OP), defined as $\Delta_{OP} = (n_{3d_{z^2}} - n_{3d_{x^2-y^2}}) / (n_{3d_{z^2}} + n_{3d_{x^2-y^2}})$, becomes less (Fig. 4e and Supplementary Note 13), that is, the $\text{Ni } 3d$ orbital mixing (OM) ($I_{OM} = 1 - \Delta_{OP}$) becomes larger. The increased orbital mixing transforms again the electronic structure of the NiO_2 planes back to more 3D-like. The middle region (Fig. 4f) with the optimal H doping is filled by the most 2D-like electronic structure that mimics the situation in cuprates and may facilitate superconductivity⁴⁰. Note that the charge inhomogeneity of $3d_{x^2-y^2}$ orbitals between NiO_4 and NiO_4H_2 environments (Supplementary Note 13) might be detrimental to superconductivity and lead to inhomogeneous superconductivity, which is another important issue for future clarification.

We highlight that the perceived picture certainly has shortcomings as DFT cannot fully capture correlation effects, which is essential for nickelate superconductors^{8,13–15}. Also, real materials are much more complex in which defects, strain and domain walls are at play that are not considered in our model. Nevertheless, our study serves as a survey of hydrogen doping effect in infinite-layer nickelates produced by topotactic reduction. An immediate next question would be, can superconductivity still be realized in these nickel oxide compounds without hydrogen or only with H doping?

Online content

Any methods, additional references, Nature Portfolio reporting summaries, source data, extended data, supplementary information, acknowledgements, peer review information; details of author contributions

and competing interests; and statements of data and code availability are available at <https://doi.org/10.1038/s41586-022-05657-2>.

- Li, D. et al. Superconductivity in an infinite-layer nickelate. *Nature* **572**, 624–627 (2019).
- Hepting, M. et al. Electronic structure of the parent compound of superconducting infinite-layer nickelates. *Nat. Mater.* **19**, 381–385 (2020).
- Crespin, M., Levitz, P. & Gatinneau, L. Reduced forms of LaNiO_3 perovskite. Part 1—evidence for new phases: $\text{La}_2\text{Ni}_2\text{O}_5$ and LaNiO_2 . *J. Chem. Soc., Faraday Trans. 2* **79**, 1181–1194 (1983).
- Katayama, T. et al. Epitaxial growth and electronic structure of oxyhydride SrVO_3H thin films. *J. Appl. Phys.* **120**, 085305 (2016).
- Tassel, C. et al. Direct synthesis of chromium perovskite oxyhydride with a high magnetic-transition temperature. *Angew. Chem. Int. Ed.* **53**, 10377–10380 (2014).
- Yajima, T. et al. A labile hydride strategy for the synthesis of heavily nitrized BaTiO_3 . *Nat. Chem.* **7**, 1017–1023 (2015).
- Yajima, T. et al. Epitaxial thin films of $\text{ATiO}_{3-x}\text{H}_x$ (A=Ba, Sr, Ca) with metallic conductivity. *J. Am. Chem. Soc.* **134**, 8782–8785 (2012).
- Poepplmeier, K. A mixed oxide-hydride perovskite. *Science* **295**, 1849–1849 (2002).
- Matsumoto, J. et al. Superconductivity at 48 K of heavily hydrogen-doped SmFeAsO epitaxial films grown by topotactic chemical reaction using CaH_2 . *Phys. Rev. Mater.* **3**, 103401 (2019).
- Zeng, S. et al. Phase diagram and superconducting dome of infinite-layer $\text{Nd}_{1-x}\text{Sr}_x\text{NiO}_2$ thin films. *Phys. Rev. Lett.* **125**, 147003 (2020).
- Li, D. et al. Superconducting dome in $\text{Nd}_{1-x}\text{Sr}_x\text{NiO}_2$ infinite layer films. *Phys. Rev. Lett.* **125**, 027001 (2020).
- Lu, H. et al. Magnetic excitations in infinite-layer nickelates. *Science* **373**, 213–216 (2021).
- Zhao, D. et al. Intrinsic spin susceptibility and pseudogaplike behavior in infinite-layer LaNiO_2 . *Phys. Rev. Lett.* **126**, 197001 (2021).
- Cui, Y. et al. NMR evidence of antiferromagnetic spin fluctuations in $\text{Nd}_{0.85}\text{Sr}_{0.15}\text{NiO}_2$. *Chin. Phys. Lett.* **38**, 067401 (2021).
- Fowlie, J. et al. Intrinsic magnetism in superconducting infinite-layer nickelates. *Nat. Phys.* **18**, 1043–1047 (2022).
- Pan, G. A. et al. Superconductivity in a quintuple-layer square-planar nickelate. *Nat. Mater.* **21**, 160–164 (2022).
- Krieger, G. et al. Charge and spin order dichotomy in NdNiO_2 driven by the capping layer. *Phys. Rev. Lett.* **129**, 027002 (2022).
- Tam, C. C. et al. Charge density waves in infinite-layer NdNiO_2 nickelates. *Nat. Mater.* **21**, 1116–1120 (2022).
- Rossi, M. et al. A broken translational symmetry state in an infinite-layer nickelate. *Nat. Phys.* **18**, 869–873 (2022).
- Gu, Q. et al. Single particle tunneling spectrum of superconducting $\text{Nd}_{1-x}\text{Sr}_x\text{NiO}_2$ thin films. *Nat. Commun.* **11**, 6027 (2020).
- Gao, Q., Zhao, Y., Zhou, X.-J. & Zhu, Z. Preparation of superconducting thin films of infinite-layer nickelate $\text{Nd}_{0.8}\text{Sr}_{0.2}\text{NiO}_2$. *Chin. Phys. Lett.* **38**, 077401 (2021).
- Zhou, X. et al. Antiferromagnetism in Ni-based superconductors. *Adv. Mater.* **34**, 2106117 (2022).
- Nakamura, S., Iwasa, N., Senoh, M. & Mukai, T. Hole compensation mechanism of P-type GaN films. *Jpn. J. Appl. Phys.* **31**, 1258–1266 (1992).
- Puphal, P. et al. Investigation of hydrogen incorporations in bulk infinite-layer nickelates. *Front. Phys.* **10**, 834682 (2022).
- Malyi, O. I., Varignon, J. & Zunger, A. Bulk NdNiO_2 is thermodynamically unstable with respect to decomposition while hydrogenation reduces the instability and transforms it from metal to insulator. *Phys. Rev. B* **105**, 014106 (2022).
- Si, L. et al. Topotactic hydrogen in nickelate superconductors and akin infinite-layer oxides ABO_2 . *Phys. Rev. Lett.* **124**, 166402 (2020).
- Ding, X. et al. Stability of superconducting $\text{Nd}_{0.8}\text{Sr}_{0.2}\text{NiO}_2$ thin films. *Sci. China-Phys. Mech. Astron.* **65**, 267411 (2022).
- Zhou, Y. et al. Real-time mass spectrometric characterization of the solid–electrolyte interphase of a lithium-ion battery. *Nat. Nanotechnol.* **15**, 224–230 (2020).
- Bang, J., Matsui, S. & Hosono, H. Hydrogen anion and subgap states in amorphous In–Ga–Zn–O thin films for TFT applications. *Appl. Phys. Lett.* **110**, 232105 (2017).
- Chen, Z. et al. Electronic structure of superconducting nickelates probed by resonant photoemission spectroscopy. *Matter* **5**, 1806–1815 (2022).
- Rossi, M. et al. Orbital and spin character of doped carriers in infinite-layer nickelates. *Phys. Rev. B* **104**, L220505 (2021).
- Higashi, K., Winder, M., Kuneš, J. & Hariki, A. Core-level X-ray spectroscopy of infinite-layer nickelate: LDA+DMFT study. *Phys. Rev. X* **11**, 041009 (2021).
- Khazaei, M. et al. Nearly free electron states in MXenes. *Phys. Rev. B* **93**, 205125 (2016).
- Lee, K., Kim, S. W., Toda, Y., Matsuishi, S. & Hosono, H. Dicalcium nitride as a two-dimensional ferulide with an anionic electron layer. *Nature* **494**, 336–340 (2013).
- Matsushita, Y.-i, Furuya, S. & Oshiyama, A. Floating electron states in covalent semiconductors. *Phys. Rev. Lett.* **108**, 246404 (2012).
- Wang, J. et al. Anomalous Dirac plasmons in 1D topological electrides. *Phys. Rev. Lett.* **123**, 206402 (2019).
- Nomura, Y. et al. Formation of a two-dimensional single-component correlated electron system and band engineering in the nickelate superconductor NdNiO_2 . *Phys. Rev. B* **100**, 205138 (2019).
- Gu, Y., Zhu, S., Wang, X., Hu, J. & Chen, H. A substantial hybridization between correlated Ni-*d* orbital and itinerant electrons in infinite-layer nickelates. *Commun. Phys.* **3**, 84 (2020).
- Shen, Y. et al. Role of oxygen states in the low valence nickelate $\text{La}_2\text{Ni}_3\text{O}_8$. *Phys. Rev. X* **12**, 011055 (2022).
- Sakakibara, H., Usui, H., Kuroki, K., Arita, R. & Aoki, H. Two-orbital model explains the higher transition temperature of the single-layer Hg-cuprate superconductor compared to that of the La-cuprate superconductor. *Phys. Rev. Lett.* **105**, 057003 (2010).

Publisher's note Springer Nature remains neutral with regard to jurisdictional claims in published maps and institutional affiliations.

Springer Nature or its licensor (e.g. a society or other partner) holds exclusive rights to this article under a publishing agreement with the author(s) or other rightsholder(s); author self-archiving of the accepted manuscript version of this article is solely governed by the terms of such publishing agreement and applicable law.

© The Author(s), under exclusive licence to Springer Nature Limited 2023

Methods

Thin films growth and characterization

Here, 15-nm-thick $\text{Nd}_{0.8}\text{Sr}_{0.2}\text{NiO}_3$ films were epitaxially fabricated on TiO_2 -terminated SrTiO_3 (001) substrates using pulsed laser deposition, at a growth temperature of 620 °C and an oxygen pressure of 200 mTorr. The real-time reflective high-energy electron diffraction intensity oscillation and pattern along the SrTiO_3 [101] azimuth direction, along with the XRD pattern, can be found in Extended Data Fig. 1. After growth, the samples were cooled down to room temperature in the same oxygen pressure at a cooling rate of 10 °C per minute. The as-grown samples were cut into pieces and wrapped in aluminium foil, then sealed together with 0.1 g of CaH_2 powder in a quartz tube (pressure <0.1 mTorr). The reduction temperature was fixed at 300 °C. The ramp rate and reduction time are illustrated in Extended Data Fig. 1d. The structure of the films was characterized using a Bruker D8 Discover diffractometer in diffraction and reflectance modes. Temperature-dependent resistivity and Hall effect were measured using the four-probe method and van der Pauw geometry in a cryogen-free magnet system (Cryogenic Ltd and Quantum Design Ltd).

Time-of-flight-secondary-ion mass spectrometry (TOF-SIMS) measurement

TOF-SIMS measurements were achieved by a TOF-SIMS-5 instrument (IONTOF GmbH) to determine the hydrogen concentration of samples. Depth profiling was done in dual beam mode by two ion beams. The pulsed analysis ion beam (Bi^+ , 30 keV), allowing a beam diameter of less than 100 nm, was digitally scanned within a $1,024 \times 1,024$ array over an analysis area of $100 \times 100 \mu\text{m}^2$ for mass spectra measurement. The spatial distribution of various elements can be mapped to this 2D image by selecting their characteristic peaks, with about 0.1 μm lateral resolution. Another pulsed low-energy sputtering ion beam (Cs^+ , 0.5 keV) was used for ablation of the surface, resulting in a crater ($300 \times 300 \mu\text{m}^2$, depth resolution better than 1 nm). The sputtering beam was interleaved with the analysis beam, with the analysis area in the centre of the crater to avoid disturbance from the crater edge. Through sequential ‘analysis-sputtering’ cycles, a series of depth-dependent 2D images was obtained. The 3D analysis is a combination of these sequential 2D image layers in the depth direction. All signals were collected by negative secondary ions.

The first several cycles were actually a surface cleaning process, after which the data collection reached equilibrium. The error bars reflect the standard error of the test, which is calculated by dividing the standard deviation by the square root of the number of measurements that make up the mean.

It is crucial to identify a good SIMS reference for quantification of H element. Although H implanted Si or SrTiO_3 were used as a reference⁴¹, the implanted H atoms are not bonded tightly to the crystal lattice and are very mobile, leading to H loss near surface region. More H loss would be caused during SIMS depth profiling, resulting in an inaccurate result. Therefore, an ideal H reference for SIMS quantification should be a solid-state material that is stable in a characterization environment with H ions bonded in the lattice. In this regard, natural mica (with a H density of 0.83×10^{22} per cm^3), $\text{KAl}_2[\text{AlSi}_3\text{O}_{10}](\text{OH})_2$, is satisfactory to these requirements⁴². By comparing with H signal in mica, we first get the maximum density of H in $\text{Nd}_{0.8}\text{Sr}_{0.2}\text{NiO}_2\text{H}_x$ thin films, and then determine the x value in the formula. Least-squares linear curve fitting was used to determine the x value in samples without SIMS measurement.

XAS and RIXS measurements

XAS and RIXS spectra near the $\text{Ni} L_3$ -edge were measured at the Beamline I21 at Diamond Light Source in the UK⁴³. All measurements were done at 20 K. The horizontal scattering plane was parallel to the

crystallographic a - c (or equivalently b - c) planes to ensure momentum transfer along the Ni-O bonds (Fig. 3a). For XAS measurements, signals were collected with a grazing incidence angle of $\theta = 20^\circ$. Total electron yield XAS spectra were collected by the drain current and normalized to the incoming beam intensity. Both linear vertical (σ) and linear horizontal polarized (π) incoming X-rays were used. For RIXS measurement, the incident X-ray energy was set to the peak of $\text{Ni} L_3$ resonance (roughly 853 eV), the scattering angle was fixed at 154° and the combined instrument resolution was about 41 meV (full-width at half-maximum).

DFT calculations

First-principles generalized gradient approximation plus U ($U = 3$ eV) calculations for $(\text{Nd}_{0.8}\text{Sr}_{0.2})\text{NiO}_2\text{H}_x$ were performed using the VASP package⁴⁴, PAW pseudopotentials⁴⁵ with the 4 f electrons treated as core electrons were used. The lattice constants of the ab plane were fixed to the SrTiO_3 substrate ($a = b = 3.905$ Å) while being relaxed in the c direction. The Sr doping effect was simulated in the spirit of virtual crystal approximation (VCA)⁴⁶. To directly show the effect of H atoms on electronic structures, all the band structures calculated in the supercells were unfolded to the unit cell. The hopping parameters for different orbitals were obtained from Wannier downfolding as implemented in Wannier90 (ref. 47). Five Ni 3 d , five Nd 5 d , three O 2 p and one IIS orbital were used to fit the DFT band structures. Eleven orbitals (five Ni 3 d , five Nd 5 d and IIS) were used to confirm the hybridization between $\text{Ni} d_{x^2-y^2}$ and IIS.

Data availability

The data that support the findings of this study are available from the Figshare data repository, https://figshare.com/articles/dataset/Critical_Role_of_Hydrogen_for_Superconductivity_in_Infinite-layer_Nickelates/21591546. Source data are provided with this paper.

Code availability

The code that supports the findings of this study is available from the corresponding author upon request.

- Lu, N. et al. Electric-field control of tri-state phase transformation with a selective dual-ion switch. *Nature* **546**, 124–128 (2017).
- Radoslovich, E. The structure of muscovite, $\text{KAl}_2(\text{Si}_3\text{Al})\text{O}_{10}(\text{OH})_2$. *Acta Crystallogr.* **13**, 919–932 (1960).
- Zhou, K.-J. et al. I21: an advanced high-resolution resonant inelastic X-ray scattering beamline at Diamond Light Source. *J. Synchrotron Rad.* **29**, 563–580 (2022).
- Kresse, G. & Furthmüller, J. Efficient iterative schemes for *ab initio* total-energy calculations using a plane-wave basis set. *Phys. Rev. B* **54**, 11169–11186 (1996).
- Blöchl, P. E. Projector augmented-wave method. *Phys. Rev. B* **50**, 17953–17979 (1994).
- Bellaiche, L. & Vanderbilt, D. Virtual crystal approximation revisited: application to dielectric and piezoelectric properties of perovskites. *Phys. Rev. B* **61**, 7877–7882 (2000).
- Pizzi, G. et al. Wannier90 as a community code: new features and applications. *J. Phys. Condens. Matter* **32**, 165902 (2020).

Acknowledgements L.Q. acknowledges the support by National Natural Science Foundation of China (grant nos. 12274061, 52072059 and 11774044), Science and Technology Department of Sichuan Province (grant nos. 2021JDJQ0015 and 2022ZYD0014) and Fundamental Research Funds for the Central Universities (grant no. ZYGX2020J023). X.S. and B.H. acknowledge the support from the NSFC (grant no. 12088101) and NSAF (grant no. U2230402). We thank Diamond Light Source for providing beam time under proposal ID NT30296. S.L. thanks Australian Research Council Discovery Projects (grant nos. DP220103229 and DP19013661) for the financial support. Computations were done at Tianhe-JK cluster at CSRC. TOF-SIMS was conducted in the University of New South Wales Mark Wainwright Analytical Centre.

Author contributions L.Q. designed the project. L.Q., K.-J.Z. and B.H. interpreted the experimental and theoretical data and supervised the project. X.D. performed thin film growth, XRD measurement, electrical properties and Hall effect characterizations. M.X. and Y.Z. helped with film growth and post-reduction. H.L. helped with electrical properties measurement. X.W. and Q.W. helped with film growth and physical property system measurements. C.C.T., J.C.,

M.G.-F., S.A. and K.-J.Z. performed XAS and RIXS measurements. J.Z. and S.L. performed SIMS measurements. M.W. and P.G. performed the transmission electron microscopy measurements. X.S. and B.H. performed DFT calculations. H.X. and X.Z. helped with DFT theory study. All the authors participated in data analysis and discussion. K.-J.Z., X.D., L.Q. and B.H. drafted the manuscript with input from all authors.

Competing interests The authors declare no competing interests.

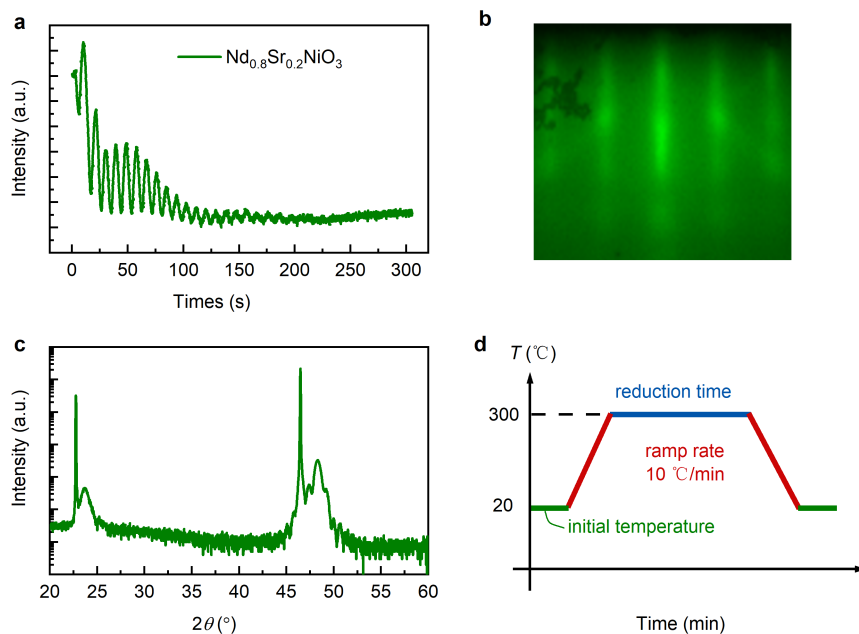
Additional information

Supplementary information The online version contains supplementary material available at <https://doi.org/10.1038/s41586-022-05657-2>.

Correspondence and requests for materials should be addressed to Qingyuan Wang, Bing Huang, Ke-Jin Zhou or Liang Qiao.

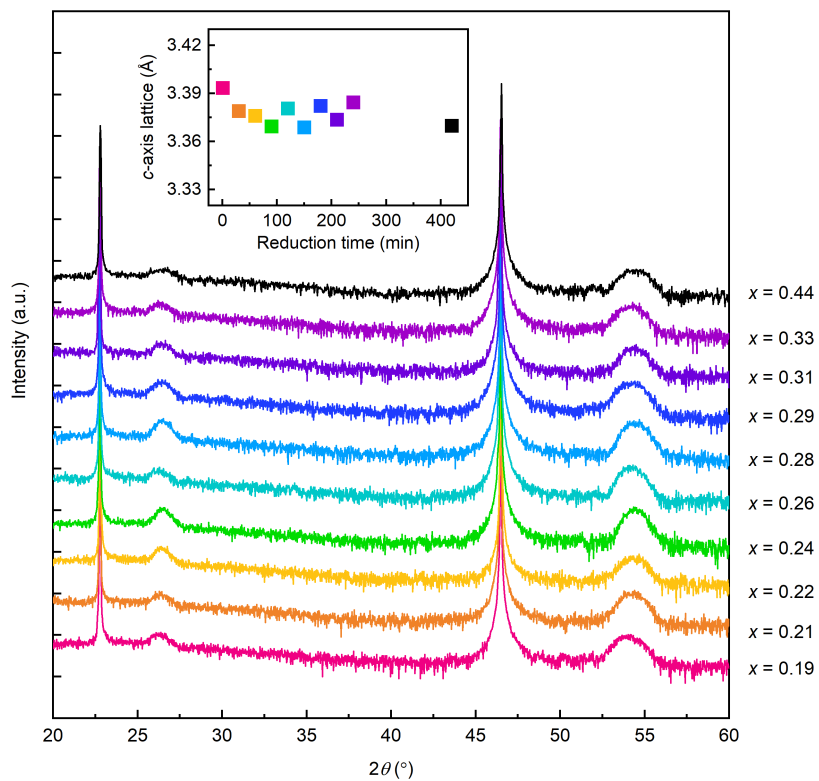
Peer review information *Nature* thanks the anonymous reviewers for their contribution to the peer review of this work.

Reprints and permissions information is available at <http://www.nature.com/reprints>.

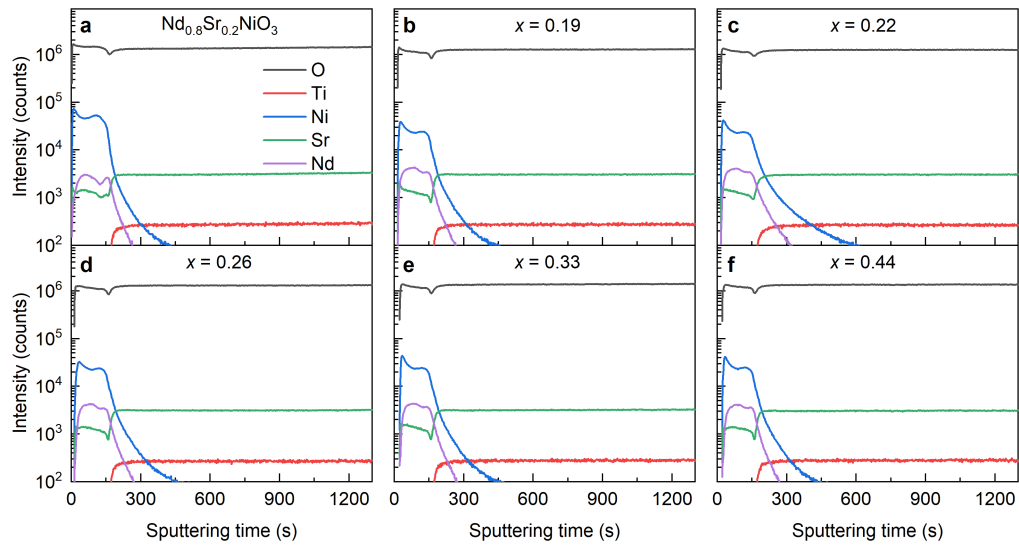


Extended Data Fig. 1 | Characterization of perovskite structure and description of topotactical reduction process. **a, b**, Typical RHEED intensity oscillation and RHEED pattern along SrTiO_3 [101] azimuth direction for $\text{Nd}_{0.8}\text{Sr}_{0.2}\text{NiO}_3$ films. The oscillations indicate that the film grows layer by layer during the initial stage of growth. The layer-by-layer growth gradually

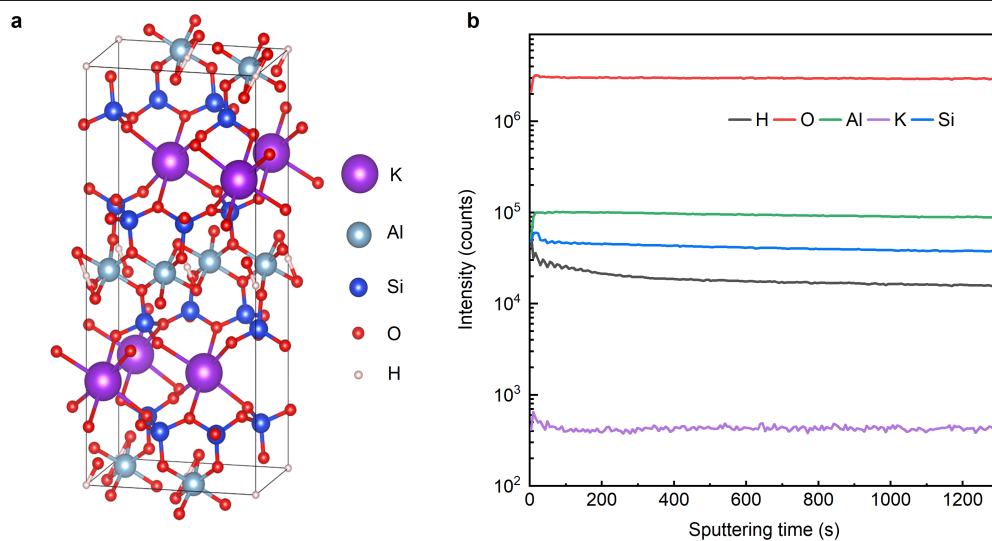
disappeared as the film thickened. **c**, Typical XRD of as-grown $\text{Nd}_{0.8}\text{Sr}_{0.2}\text{NiO}_3$ films. $\text{Nd}_{0.8}\text{Sr}_{0.2}\text{NiO}_3$ (001) and (002) diffraction peaks are located at 23.7° and 48.3° , respectively. **d**, Illustration of the reduction heating process. During the reduction time the sample is maintained at the temperature of $300\text{ }^\circ\text{C}$.



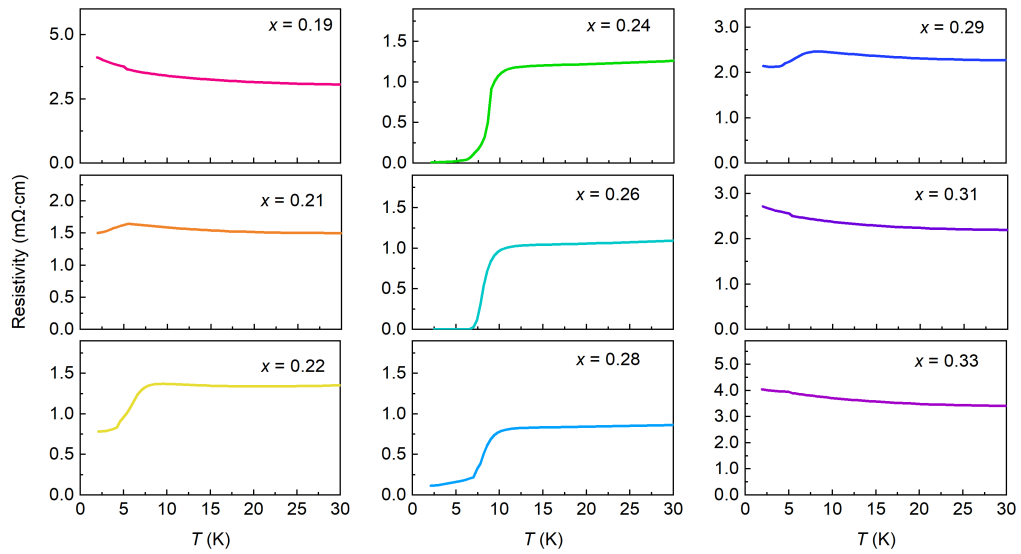
Extended Data Fig. 2 | X-ray diffraction for all $\text{Nd}_{0.8}\text{Sr}_{0.2}\text{NiO}_2\text{H}_x$ films. XRD scans of films with reduction time varied from 1 min to 420 min. The insert picture shows the corresponding c lattice parameters.



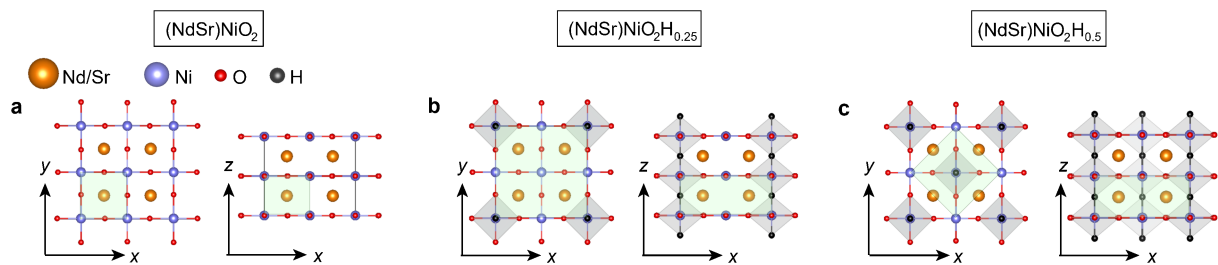
Extended Data Fig. 3 | SIMS spectra of other elements in thin film and substrate. SIMS signals of O, Ti, Ni, Sr, Nd secondary ions in the films under different H doping levels.



Extended Data Fig. 4 | Crystal structure and SIMS spectrum of mica. **a**, Crystal structure of mica with the formula of $\text{KAl}_2[\text{AlSi}_3\text{O}_{10}](\text{OH})_2$. **b**, SIMS spectrum of H, O, Al, K, Si secondary ions in mica as a reference sample for calibration.

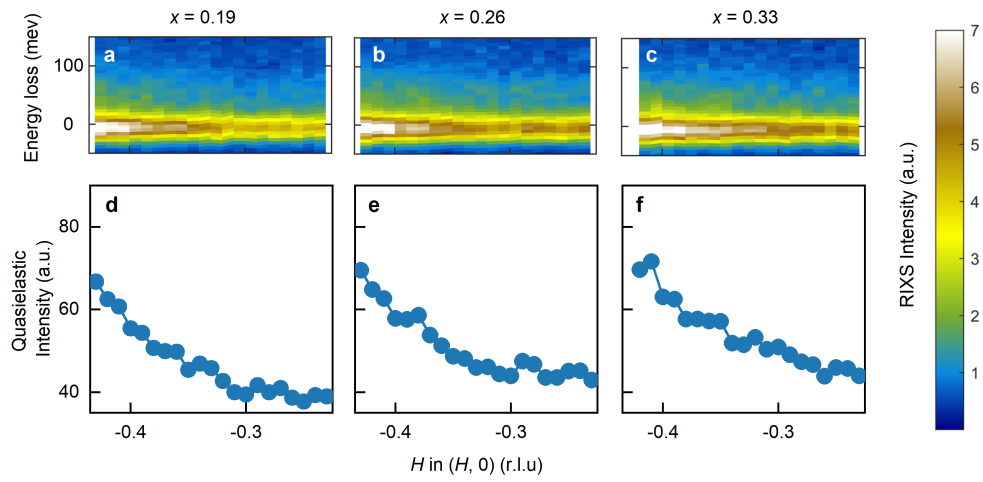


Extended Data Fig. 5 | Zoom-in view of $\rho(T)$ with different H concentrations. The temperature-dependent resistivities of $\text{Nd}_{0.8}\text{Sr}_{0.2}\text{NiO}_2\text{H}_x$ films with x varying from 0.19 to 0.33.



Extended Data Fig. 6 | Crystal structure of $\text{Nd}_{0.8}\text{Sr}_{0.2}\text{NiO}_2\text{H}_x$. a-c, Lowest energy configurations of $\text{Nd}_{0.8}\text{Sr}_{0.2}\text{NiO}_2\text{H}_x$ ($x = 0, 0.25$ and 0.5) in $2 \times 2 \times 2$ supercell, where H forms 1D chain structure along c direction [see details in

Supplementary Note 12]. The green shaded areas indicate the unit cells. These structures are used for electronic structure calculations in Fig. 4.



Extended Data Fig. 7 | RIXS spectra of $\text{Nd}_{0.8}\text{Sr}_{0.2}\text{NiO}_{2}\text{H}_x$. Low-energy RIXS intensity maps (a-c) and the integrated quasielastic region (d-f) of three $\text{Nd}_{0.8}\text{Sr}_{0.2}\text{NiO}_{2}\text{H}_x$ samples with $x = 0.19$ (a, d), 0.26 (b, e) and 0.33 (c, f), respectively. No sign of CDWs is present in any probed samples.

Extended Data Table 1 | Hopping energy t and onsite energy difference Δ (in units of eV) without and with the insertion of H in $\text{Nd}_{0.8}\text{Sr}_{0.2}\text{NiO}_2\text{H}_x$ ($x=0.25$)

	t_1	t_2	t_3	t_4
w/o H	1.32	-0.63	-0.21	0.23
w H	1.32	0	0	0.06

	Δ_1	Δ_2	Δ_3	Δ_4
w/o H	3.89	6.67	2.78	3.12
w H	3.81	--	--	2.94

These values are insensitive to the H doping.